Chemical Science

EDGE ARTICLE

View Article Online
View Journal | View Issue

Cite this: *Chem. Sci.*, 2019, **10**, 2796

All publication charges for this article have been paid for by the Royal Society of Chemistry

Electrocatalytic water oxidation over $AlFe_2B_2$†

Dallas K. Mann,‡[a] Junyuan Xu,‡[b] Natalia E. Mordvinova,[c] Vincent Yannello,[a] Yasmine Ziouani,[b] Noelia González-Ballesteros,[d] Juliana P. S. Sousa,[b] Oleg I. Lebedev,[c] Yury V. Kolen'ko *[b] and Michael Shatruk *[a]

Received 14th September 2018
Accepted 15th January 2019

DOI: 10.1039/c8sc04106g

rsc.li/chemical-science

We report excellent electrocatalytic performance by $AlFe_2B_2$ in the oxygen-evolution reaction (OER). The inexpensive catalytic material, prepared simply by arc-melting followed by ball-milling, exhibits high stability and sustained catalytic performance under alkaline conditions. The overpotential value of 0.24 V observed at the current density of 10 mA cm^{-2} remained constant for at least 10 days. Electron microscopy and electron energy loss spectroscopy performed on the initial ball-milled material and on the material activated under electrocatalytic conditions suggest that the catalytic mechanism involves partial leaching of Al from the layered structure of $AlFe_2B_2$ and the formation of Fe_3O_4 nanoclusters on the exposed $[Fe_2B_2]$ layers. Thus, the $AlFe_2B_2$ structure serves as a robust supporting material and, more importantly, as a pre-catalyst to the *in situ* formed active electrocatalytic sites. Comparative electrochemical measurements demonstrate that the electrocatalytic performance of the $AlFe_2B_2$-supported Fe_3O_4 nanoclusters substantially exceeds the results obtained with unsupported nanoparticles of Fe_3O_4, FeB, or such benchmark OER catalysts as IrO_2 or RuO_2. The excellent catalytic performance and long-term stability of this system suggests that $AlFe_2B_2$ can serve as a promising and inexpensive OER electrocatalyst.

Introduction

Fast depletion of fossil fuels drives extensive research efforts aimed at the development of renewable energy sources.[1] Solar-powered fuel cells are one of the desired clean-energy technologies, which rely on the utilization of sun and water as renewable energy sources.[2] Water electrolysis can be divided into two half reactions, hydrogen evolution reaction (HER) and oxygen evolution reaction (OER). In practice, the overall voltage required for electrocatalytic water splitting is substantially larger than the minimum thermodynamic value of 1.23 V. The excess voltage, known as overpotential, is due to various kinetic factors involved in the HER and OER processes.[3] The goal of electrocatalysis is to decrease the overpotential and afford more energy-efficient water splitting.

The extensive several-decade body of research into the HER and OER electrocatalysts[4] suggests some important criteria for the development of new catalytic systems: (1) for practical implementation, the catalyst should be heterogeneous; (2) to offer a viable alternative to fossil fuels, the catalyst should be inexpensive and composed of earth-abundant elements; (3) the catalyst should exhibit long-term chemical stability under extreme catalytic conditions; (4) the catalyst should combine active catalytic sites with a robust support for uninterrupted performance with high turnover frequency (TOF).

The state of the art electrocatalysts for HER and OER are Pt and IrO_2 or RuO_2, respectively.[5] These catalysts are based on platinum group metals (PGMs), which are expensive and limited in their reserves. To that end, many recent works have focused on the investigation of electrocatalysts that incorporate first-row transition metals.[4d,5,6] Providing a high surface area conductive support for the deposition of active catalyst nanoparticles is a widely accepted method for achieving heterogeneous catalysis and improving the long-term stability of the nanoscaled catalyst. For example, CoO_x, one of the best catalysts for electrolytic water splitting, shows excellent performance in the presence of phosphate anions, which allegedly promote the formation of a supported and self-healing catalyst structure with easily accessible catalytic sites.[4c]

An alternative strategy for achieving a supported catalyst with high surface area uses "multicomponent" materials, in which different parts of the structure can serve as the active catalytic sites and the inert conductive support. Such architecture allows the implementation of the active site separation concept, which has been shown to be effective in a number of intermetallic catalysts. As an example of this strategy, AlMoB

[a]*Department of Chemistry and Biochemistry, Florida State University, 95 Chieftan Way, Tallahassee, FL 32306, USA. E-mail: shatruk@chem.fsu.edu*

[b]*International Iberian Nanotechnology Laboratory, Braga 4715-330, Portugal. E-mail: yury.kolenko@inl.int*

[c]*Laboratoire CRISMAT, UMR 6508, CNRS-Ensicaen, Caen 14050, France*

[d]*Inorganic Chemistry Department, Biomedical Research Centre (CINBIO), Universidade de Vigo, Vigo 36210, Spain*

† Electronic supplementary information (ESI) available. See DOI: 10.1039/c8sc04106g

‡ Both authors contributed equally to this manuscript.

has been recently reported as an efficient HER electrocatalyst.[7] The material showed high stability under acidic conditions. In addition, it was found that the catalytic performance improved when the material was pre-etched under basic conditions. In alkaline solution, the Al atoms sandwiched between the MoB layers are etched away to open up the catalytically active transition metal sites that subsequently catalyze HER.[8] The underlying structure of AlMoB thus acts as a robust conductive support for the catalytically active sites separated by the partially etched Al layers.

The crystal structure of AlMoB (Fig. 1a) has attracted our attention due to its similarity with the structure of another ternary intermetallic compound, $AlFe_2B_2$ (Fig. 1b), which we earlier explored as a promising magnetocaloric material.[9] We have hypothesized that similar Al-etching procedure can affect the layered structure of $AlFe_2B_2$ by exposing the $[Fe_2B_2]$ layers for the subsequent electrocatalytic reaction. Indeed, a theoretical analysis presented herein demonstrates that the bonding between the Al and $[Fe_2B_2]$ layers in this structure is substantially weaker than the Fe–B and B–B bonds within the $[Fe_2B_2]$ layer. We have also recently reported *in situ* formation of highly active nickel oxide nanocluster OER electrocatalysts from nickel phosphide scaffolds.[10] By analogy with the binary Ni–P, we hypothesized that $[Fe_2B_2]$ layers could serve as an interesting precursor for Fe-based OER electrocatalyst. This hypothesis is followed by an experimental demonstration that $AlFe_2B_2$ affords efficient OER with a low overpotential and remarkably high stability of the electrocatalyst. A comprehensive investigation of the electrocatalytic process reveals that $AlFe_2B_2$ acts as a robust scaffold for *in situ* formation of catalytically active Fe_3O_4 nanoclusters on the surface of the $[Fe_2B_2]$ layers. The excellent catalytic performance and long-term stability coupled to the convenient synthesis suggest that this system can serve as a promising and inexpensive OER electrocatalyst.

Materials and methods

Synthesis

All manipulations during sample preparation were carried out in an Ar-filled dry box (content of O_2 < 0.5 ppm). Powders of aluminum (99.97%), iron (98%), crystalline boron (98%), and iron boride (FeB, 98%) were obtained from Alfa Aesar. The iron powder was additionally purified by heating in a flow of H_2 gas at 500 °C for 5 h. The other materials were used as received.

$AlFe_2B_2$ was synthesized as previously reported.[9] Starting materials were mixed in a Al : Fe : B = 3 : 2 : 2 ratio (a total weight of 0.35 g) and pressed into a pellet, which was arc-melted in an argon-filled glovebox. The pellet was re-melted 4 times to achieve uniform melting. To maximize the sample's homogeneity, it was sealed in a silica tube under vacuum ($\sim 10^{-5}$ Torr) and annealed at 900 °C for 1 week. The annealed sample was ground and subjected to powder X-ray diffraction (PXRD), which revealed $AlFe_2B_2$ as the major phase and $Al_{13}F_4$ as a minor byproduct. The latter was removed by treating the sample for 3–5 min with dilute (1 : 1 v/v) aqueous solution of HCl.

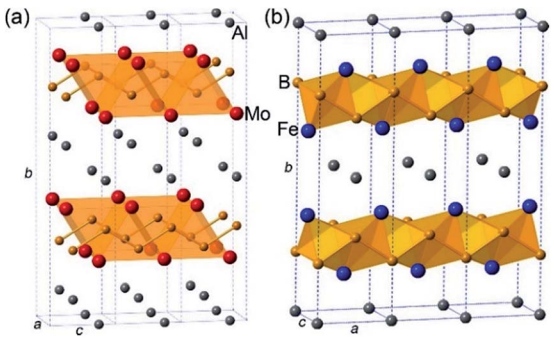

Fig. 1 The crystal structures of AlMoB (a) and $AlFe_2B_2$ (b).

Powder X-ray diffraction

Room-temperature PXRD was carried out on a Panalytical X'Pert Pro diffractometer with an X'Celerator detector using Cu-Kα radiation (λ = 1.54187 Å). Each pattern was recorded in the 2θ range of 10° to 80° with a step of 0.05° and the total collection time of 1 h. The analysis of PXRD patterns was carried out with the HighScore Plus software (Panalytical).[11]

Electrocatalyst preparation

The phase-pure sample of $AlFe_2B_2$ was ball-milled at 1725 rpm for 1 h in an 8000 M High-Energy Mixer/Mill (SPEX), using a stainless-steel ball-milling set. The milling was carried out under Ar to minimize surface oxidation. The PXRD of the ball-milled sample revealed broadening of diffraction peaks, in accord with the decreased particle size. No traces of impurity phases were observed, except for a minor peak of Al_2O_3 (which will be dissolved under basic conditions of electrochemical testing). Specific surface areas (S_{BET}) of the as-prepared $AlFe_2B_2$ and reference catalysts were estimated using the Brunauer–Emmett–Teller (BET) model with the Autosorb iQ_2 analyzer (Quantachrome). The ball-milled sample of $AlFe_2B_2$ was converted into an electrocatalyst ink by ultrasonically dispersing 5 mg of the material in 1000 μL of ethanol containing 50 μL of a Nafion solution (Sigma-Aldrich, 5 wt%). To prepare an electrode for catalytic tests, 200 μL of the ink was loaded on a Ni foam (Heze Jiaotong, 110 pores per inch, 0.3 mm thick, cleaned by ultrasonication in 6 M HCl) with an exposed area of 1.0 cm^2, leading to a loading density of $\sim$1.0 mg cm^{-2}. The electrode was then allowed to dry naturally under ambient conditions.

Electrochemical measurements

Electrochemical measurements were conducted at 25 °C, using a Biologic VMP-3 potentiostat/galvanostat. The OER performance of various catalysts was evaluated in a three-electrode system using 1.0 M KOH electrolyte, in which the catalytic electrode, the saturated calomel electrode (SCE), and a Pt wire served as the working, reference, and counter electrodes, respectively. Prior to each measurement, the SCE electrode was calibrated in Ar/H_2-saturated 0.5 M H_2SO_4 solution, using a clean Pt wire as the working electrode. Unless stated otherwise, all potentials reported in this work were converted to

a reversible hydrogen electrode (RHE) reference scale according to the following equation: $E_{RHE} = E_{SCE} + 0.059pH + 0.241$. An *iR*-correction of 85% was applied in the polarization experiments to compensate for the voltage drop between the reference and working electrodes, which was evaluated by a single-point high-frequency impedance measurement.

OER anodic polarization curves were recorded with a scan rate of 5 mV s^{-1} in the range from 1.0 to 1.7 V *vs.* RHE. Impedance spectroscopy measurements were carried out at the overpotential of 0.26 V in the frequency range from 10^5 to 10^{-2} Hz with a 10 mV sinusoidal perturbation. The catalytic stability of the electrodes was evaluated as a function of time at constant current density of 10 mA cm^{-2}.

Calculation of turnover frequencies (TOFs)

The O_2 TOFs for the electrocatalysts were estimated as TOF (s^{-1}) = $(jA)/(4Fn)$, where j is the current density (A cm^{-2}) at a given overpotential, A is the surface area of the electrode (1.0 cm^2), F is the Faraday constant (96 485 C mol^{-1}), and n is the amount of metal in the electrode (mol), determined as $n = 1.0$ mg $cm^{-2} \times 1.0$ $cm^2 \times 10^{-3}$/metal molar mass. We assumed that all of the metal ions were catalytically active and thereby calculated their TOFs. Notably, some metal sites were indeed inaccessible during OER, and thus the calculated TOFs represent the minimum possible values.

Transmission electron microscopy

The transmission electron microscopy (TEM), high-angle annular dark-field scanning TEM (HAADF-STEM), electron diffraction (ED), energy-dispersive X-ray spectroscopy (STEM-EDX) and electron energy loss spectroscopy (STEM-EELS) in STEM mode studies were performed using a JEM-ARM200F microscope (cold field-emission gun, probe and image aberration corrected, equipped with CENTURIO EDX detector and GIF Quantum). TEM samples were prepared by crushing a sample in an agate mortar in ethanol and depositing the obtained suspension on a Cu carbon holey grid.

Quantum-chemical calculations

Density-functional band structure calculations and crystal orbital Hamilton population (COHP) analysis[12] were performed using the tight binding-linear muffin tin orbitals-atomic sphere approximation (TB-LMTO-ASA) software.[13] Published structural parameters of $AlFe_2B_2$ were used[14] with no theoretical geometry optimization. Fe 4s, 3d, and 4p, Al 3s, 3p, and 3d, and B 2s, 2p, and 3d states were treated as valence orbitals (with Al and B 3d states downfolded). No additional empty spheres were needed to reach an overlap volume of 8.731%. A 23 × 6 × 23 k-point mesh was used to generate COHP curves for five shortest interatomic contacts.

Results and discussion

Synthesis and analysis of $AlFe_2B_2$

As shown by us previously, phase-pure $AlFe_2B_2$ can be synthesized by means of arc-melting followed by homogenizing annealing at 900 °C. A short treatment of the annealed sample with diluted HCl is required to eliminate the minor $Al_{13}Fe_4$ impurity. The as-prepared $AlFe_2B_2$ was ball-milled for 1 h to maximize the surface area of the material. The PXRD pattern of the ball-milled sample revealed that the phase composition of the material had been preserved after ball-milling, although a minor peak observed at $2\theta = 37°$ suggests the appearance of Al_2O_3 byproduct. The impurity, however, was readily dissolved under the electrochemical testing conditions (pH = 14) used in this work. The PXRD analysis also revealed broadening of diffraction lines in the pattern of the ball-milled sample as compared to the bulk sample (Fig. 2). Analysis of the line broadening effect was carried out using the Scherrer equation,[15] which relates the average particle size (D) to the line broadening ($\Delta(2\theta)$) at various diffraction angles (θ): $D = K\lambda/[\Delta(2\theta) \times \cos\theta]$. The shape factor K was set to 0.9, and Si powder was used as a standard to evaluate the intrinsic line broadening of the diffractometer. This analysis led to $D \approx 25$ nm, indicating the substantial decrease in the crystallite size as compared to the bulk sample, as desired for electrocatalytic studies. This estimate, however, does not account for the line broadening due to strain introduced by ball-milling. Thus, it provides only the lower bound for the particle size, as will be demonstrated below by electron microscopy.

In our previous work on bulk $AlFe_2B_2$, we observed that this material also dissolves in dilute HCl (although slower than the $Al_{13}Fe_4$ impurity). Given the much higher stability of the binary FeB under acidic conditions,[16] one might assume that the reactivity of $AlFe_2B_2$ toward the acid is initiated by leaching of Al from the space between the $[Fe_2B_2]$ layers. This assumption is also supported by the fact that the Al–Fe (2.622 Å) and Al–B (2.430 Å) bond lengths are substantially longer than the bonds within the $[Fe_2B_2]$ layer (B–B at 1.605 Å and Fe–B at 2.048 and 2.199 Å).

To evaluate more quantitatively the strengths of the bonds in the $AlFe_2B_2$ structure, we carried out quantum-mechanical calculations to obtain the COHP curves for each of the aforementioned interatomic contacts. Integrating the –COHP curves, shown in Fig. 3, up to the Fermi energy (E_F) gives –ICOHP (Table 1), an energy value which correlates with the bond

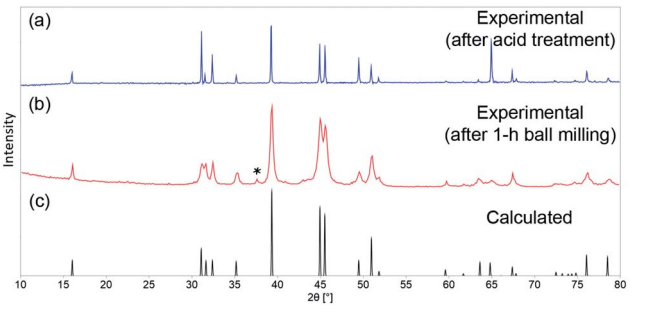

Fig. 2 PXRD patterns for the samples of $AlFe_2B_2$ obtained after arc-melting and homogenizing annealing (a) and after ball-milling under Ar atmosphere for 1 h (b). The minor Al_2O_3 impurity peak is labeled with an asterisk. The calculated PXRD pattern of $AlFe_2B_2$ is shown for comparison (c).

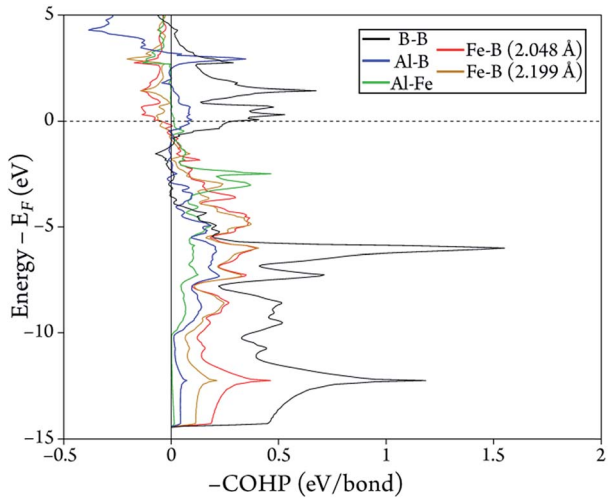

Fig. 3 Calculated –COHP curves for the five shortest interatomic contacts in the crystal structure of $AlFe_2B_2$.

Table 1 Distances and –ICOHP values calculated for the five shortest interatomic contacts in the structure of $AlFe_2B_2$

Bond	Distance (Å)	–ICOHP (eV/bond)
B–B	1.605	5.13
Al–Fe	2.622	1.02
Al–B	2.430	1.06
Fe–B	2.048	2.75
	2.199	2.15

strength.[12] The positive values of –ICOHP represent a negative energy term, which indicates an overall stabilizing interaction, while the negative values indicate destabilizing interaction. As expected, the B–B bonds are the strongest in the structure, while the two crystallographically unique Fe–B contacts are moderately strong. The weakest interactions are observed for the Al–Fe and Al–B contacts. As will be shown below, this finding agrees not only with our chemical intuition, but also with experimental results.

Electrocatalytic studies

The nanoparticles of $AlFe_2B_2$ obtained by ball-milling were converted into a catalyst ink and loaded on a Ni foam current collector. This electrocatalytic assembly was evaluated in 1 M KOH electrolyte, revealing high OER activity of the $AlFe_2B_2$ electrocatalyst. Specifically, the current densities of 10, 100, and 300 mA cm^{-2} were achieved at remarkably low overpotentials (η) of only 240, 290, and 320 mV, respectively. For comparison, we evaluated (under the same conditions) the bare Ni foam and four other control catalysts, FeB (S_{BET} = 43 m^2 g^{-1}), Fe_3O_4 (S_{BET} = 74 m^2 g^{-1}),[17] RuO_2 (S_{BET} = 11 m^2 g^{-1}), and IrO_2 (S_{BET} = 2 m^2 g^{-1}). As can be seen from Fig. 4a, when considering the activity based on the current density by electrode surface area, $AlFe_2B_2$ exhibits substantially lower overpotentials at all current densities, outperforming all the reference systems. Further comparisons of the catalytic performance normalized by S_{BET}[18] shows that $AlFe_2B_2$ demonstrates the strongest catalytic current on anodic polarization, and only IrO_2 has higher activity than the $AlFe_2B_2$-based anode (Fig. S1†).

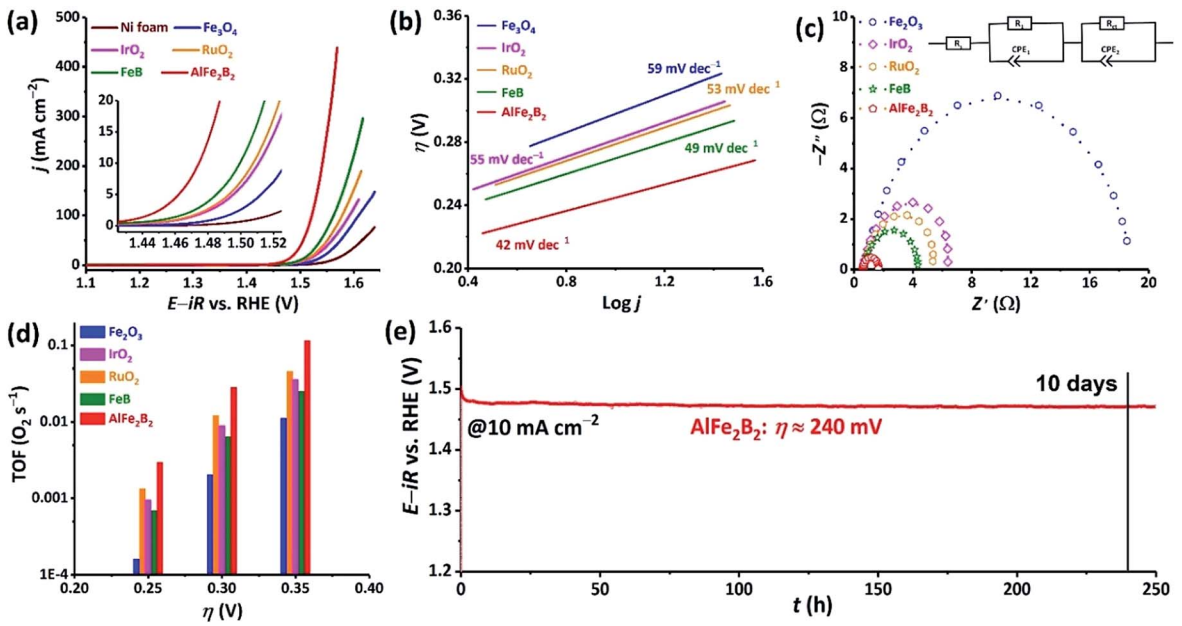

Fig. 4 Performance of different OER electrocatalysts in a 1 M KOH electrolyte solution: (a) the current density *vs.* applied potential curves, with the inset showing an enlarged low-current part of the plot. (b) The Tafel plot, showing the overpotential as a function of logarithmic current density. The numbers indicate slopes of the corresponding linear fits. (c) The Nyquist complex-plane impedance plot with the equivalent electrical circuit model shown in the inset. (d) The TOF plot at overpotentials of 0.25, 0.30, and 0.35 V. (e) The chronopotentiometric plot of the performance of $AlFe_2B_2$ electrocatalyst at the constant current density of 10 mA cm^{-2}.

The kinetic behavior of the electrocatalysts was compared by means of Tafel and Nyquist plots. The Tafel plot relates the rate of the electrochemical reaction to the overpotential by revealing the dependence of η on the logarithmic current density: $\eta = T_S \log(j/j_0)$. The Tafel slope (T_S) derived from this dependence indicates how susceptible the reaction rate is to changes in the applied voltage. The Tafel plots in Fig. 4b show that $AlFe_2B_2$ exhibits not only the lowest overpotential per geometric area but also the smallest T_S value in comparison to the reference electrocatalysts. An impressive T_S value of 42 mV dec^{-1}, determined for $AlFe_2B_2$, indicates the fastest OER rate in the 1 M KOH electrolyte. The Nyquist plot, obtained from the AC impedance measurements, also demonstrates a significantly smaller charge-transfer resistance for $AlFe_2B_2$ as compared to the reference electrocatalysts (Fig. 4c).

The O_2 TOFs were examined at various overpotentials (Fig. 4d). $AlFe_2B_2$ shows a TOF value of 0.12 s^{-1} at the overpotential of 350 mV, at which the OER benchmarks RuO_2 and IrO_2 achieved substantially lower TOFs values of 0.05 s^{-1} and 0.04 s^{-1}, respectively.

Lastly, we observed excellent stability of the $AlFe_2B_2$ electrocatalyst under the harsh OER conditions. More specifically, under the constant current density of 10 mA cm^{-2}, in the 1 M KOH electrolyte solution, $AlFe_2B_2$ maintained an essentially constant overpotential of 240 mV for over a 10 day period. Overall, our electrochemical studies establish $AlFe_2B_2$ as a highly active and inexpensive OER electrocatalyst with the remarkable long-term stability.

Upon examination of the catalyst's stability plot, we also noticed an obvious decrease in the overpotential value in the very beginning of the reaction (Fig. 4e). To further explore this feature, we carried out several electrocatalytic cycles and monitored the current–potential curves, which revealed that the electrocatalyst was becoming more active, exhibiting progressively lower overpotential upon the initial cycling (Fig. 5). As can be seen from these results, the overpotential appeared to stabilize after the first 20 cycles. To obtain a better insight into the origin of such behavior, we examined both the initial and activated catalysts by means of electron microscopy.

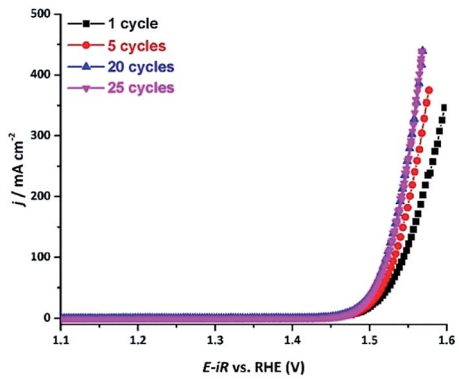

Fig. 5 The current density *vs.* applied potential curves recorded over the $AlFe_2B_2$/Ni-foam electrocatalyst after OER catalytic cycles in a 1 M KOH electrolyte solution.

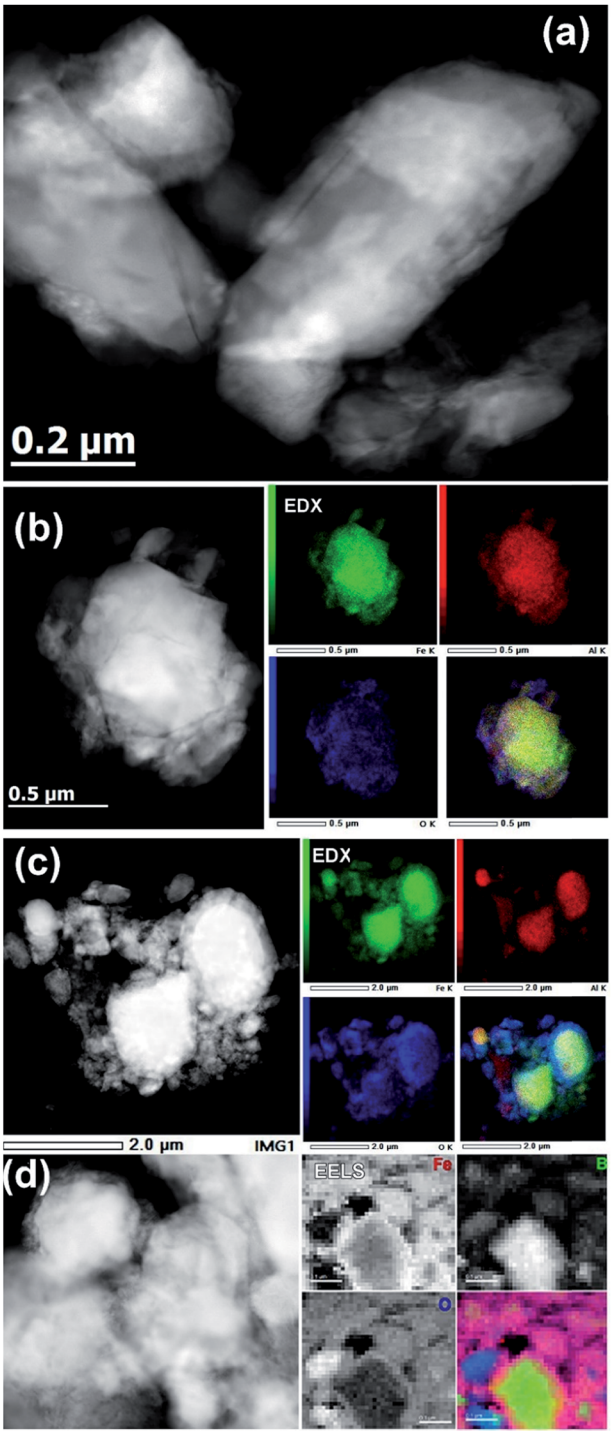

Fig. 6 HAADF-STEM images and the corresponding STEM-EDX elemental maps of $AlFe_2B_2$ particles before (a, b) and after (c) electrocatalytic activation in a 1 M KOH solution. The growth of the shell structure in the electrocatalytically activated sample can be clearly seen by comparing the EDX elemental maps shown in panels (b) and (c), where the element distribution is shown with green (Fe), red (Al), and blue (O) colors. Panel (d) shows the EELS mapping of the electrocatalytically activated sample. In the grayscale panels, lighter areas indicate a higher content of the corresponding element. The colored overlay shows the EELS signals for the B-K (green), Fe-$L_{2,3}$ (red), and O-K (blue) edges.

Electron microscopy

The TEM investigation showed that the original ball-milled sample contained particles of different sizes, ranging from ~30 nm to ~500 nm (Fig. 6a). The EDX spectroscopy showed the Al : Fe ratio of approximately 1 : 2, in agreement with the composition of the bulk material. The elemental mapping also showed the presence of a thin oxide layer (Fig. 6b), which agrees with the minor oxidation and the presence of a peak that belongs to Al_2O_3 in the PXRD pattern of the ball-milled material (Fig. 2b).

The activated sample, obtained after 20 initial OER cycles, appeared much more heterogeneous, which made its analysis difficult. Nevertheless, the overall appearance of this sample clearly revealed the formation of a core–shell structure. In comparison to the sample before the catalysis (Fig. 6b), the EDX elemental mapping showed the presence of a thick layer of iron oxide on the surface of the catalytically activated $AlFe_2B_2$ particles (Fig. 6c). The EDX elemental mapping also showed that the Al : Fe ratio had drastically decreased, from 1 : 2 in the initial catalyst to 1 : 6 in the activated one. This finding suggests that Al is partially leached out of the layered $AlFe_2B_2$ structure under the harsh basic conditions of electrocatalysis, a hypothesis supported by our theoretical analysis of the relative bond strengths (Table 1).

EELS was used to probe the changes in the nature of the Fe sites during OER and to confirm the presence and localization of boron, which is difficult to detect by EDX spectroscopy. Importantly, we observed that B was consistently present in the core–shell structures (Fig. 6d), along with Fe. Recording the combined EELS elemental map required the choice of a specific energy window to monitor the presence of different elements. Nevertheless, the EELS mapping observed in Fig. 6d clearly shows the appearance of the $AlFe_2B_2$ nanoparticles (seen as the light yellow-green colored area) shelled with a layer of iron oxide (seen as a pink shell due to the combination of red (Fe) and blue (O) colors). Furthermore, a careful look at the figure also allows us to distinguish yellow-greenish areas hidden underneath the pink areas, in agreement with the *in situ* formation of the iron oxide layer around the $AlFe_2B_2$ particles.

Taking into account the EDX results and combining them with the EELS data, we can conclude that these particles, indeed, consist of the $AlFe_2B_2$ core shelled with a layer of iron oxide. Analysis of the EELS data indicates that prior to catalytic testing the $AlFe_2B_2$ particles mainly contain Fe^0 sites, with minor Fe^{3+} impurities. After activation, the thick oxide shell appears to be magnetite, Fe_3O_4. This phase can be distinguished from α-Fe_2O_3 and FeO by examining the iron L-edge and oxygen K-edge EELS fine structure observed in the energy regions around 705–725 eV and 530–570 eV, respectively (Fig. 7). In particular, the Fe L_3 peak is shifted to lower energies as compared to the peak of α-Fe_2O_3, while the Fe L_2 peak is shifted to higher energies as compared to the peak of FeO. The formation of Fe_3O_4 nanoparticles was also confirmed by selected area ED patterns and HRTEM imaging (Fig. 8). The ED patterns were perfectly indexed using the unit cell parameters of

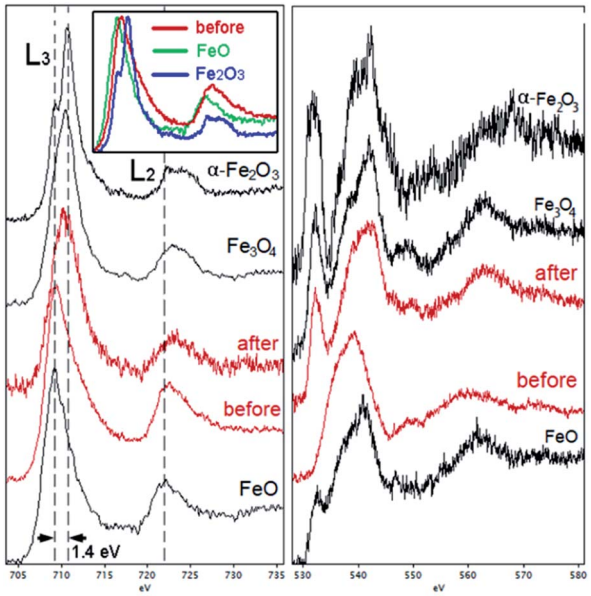

Fig. 7 Fe-$L_{2,3}$ edge (left) and O-K edge (right) EELS spectra of $AlFe_2B_2$ particles before and after electrocatalytic activation. The reference spectra of α-Fe_2O_3, Fe_3O_4, and FeO are shown for comparison.

Fe_3O_4, while the Fourier transform (FT) of the HRTEM image produced an identical ring diffraction pattern with the pronounced (111) spots characteristic of Fe_3O_4.

We should also point out that examination of the EDX spectra did not reveal any visible traces of Ni (Fig. S2†), which excludes the possibility that the high catalytic activity of our sample could be due to the formation of mixed Ni–Fe oxyhydroxides, known to be excellent OER electrocatalysts.[19]

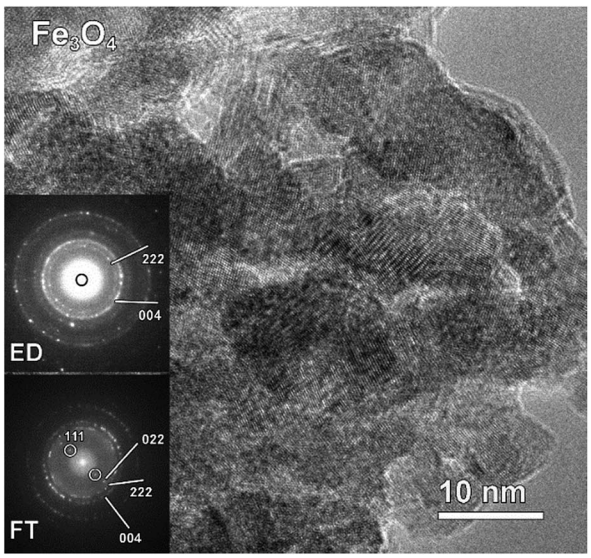

Fig. 8 HRTEM image of the activated electrocatalyst and the corresponding ED and FT ring patterns, which were indexed with the unit cell parameters of Fe_3O_4. The characteristic (111) spots observed in the FT pattern are absent in the ED pattern due to preferential orientation of the nanoparticles.

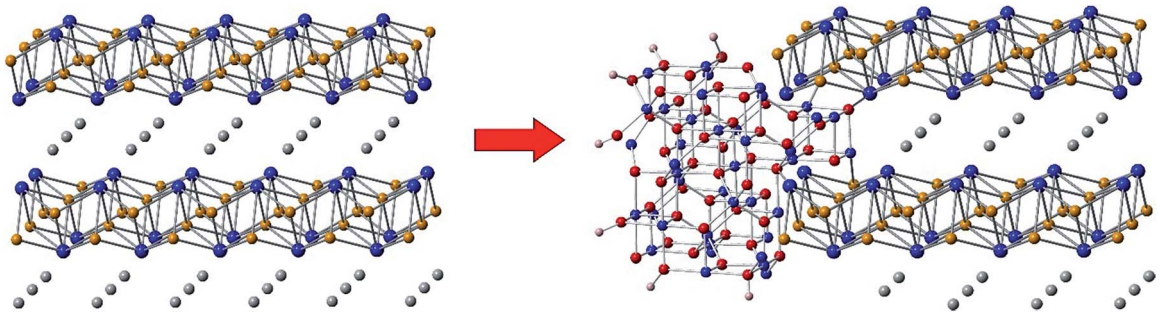

Fig. 9 Hypothesized structure of the electrocatalyst formed from the $AlFe_2B_2$ scaffold. The partial etching of Al atoms (gray) in alkaline electrolyte exposes the $[Fe_2B_2]$ layers (Fe = blue, B = orange), which are subsequently surface-oxidized to afford the formation of a shell composed of electrocatalytically active Fe_3O_4 nanoclusters (O = red).

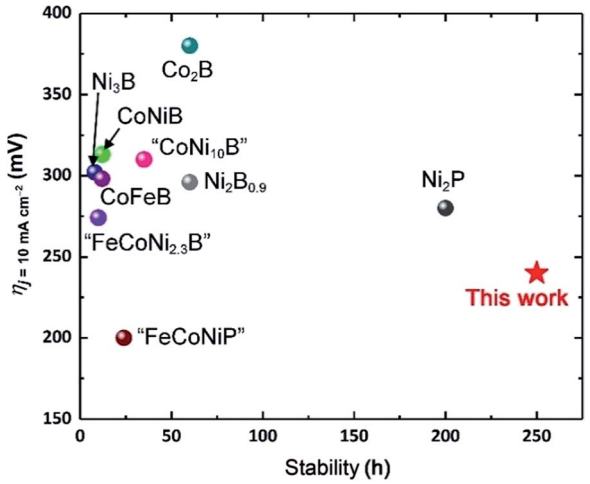

Fig. 10 Comparison of OER electrocatalytic activity and stability of previously reported boride- and phosphide-based systems[10a,21] to the performance of the $AlFe_2B_2$-based electrocatalytic system.

Based on these results, we propose that the excellent OER performance by $AlFe_2B_2$ is due to the partial etching of Al from the structure, followed by the surface oxidation of the exposed $[Fe_2B_2]$ layers, as reflected by the following idealized reaction sequence:

$$2AlFe_2B_2 + 2KOH + 6H_2O = 2K[Al(OH)_4] + 4\text{“FeB”} + 3H_2,$$

$$12\text{“FeB”} + 6KOH + 17O_2 = 3K_2B_4O_7 + 4Fe_3O_4 + 3H_2O,$$

where “FeB” stands for the modified $AlFe_2B_2$ with partially etched Al layers.

We would like to emphasize that the scheme shown above provides a much simplified version of the surface reconstruction process, which likely involves (a) the dissolution of the Al layers; (b) the formation of hydroxidic Fe species due to the oxidation of the $[Fe_2B_2]$ layers under alkaline conditions; (c) the diffusion of oxygen through the shell of oxidized Fe species, leading to gradual thickening of the shell and conversion of its bulk to Fe_3O_4. The formation of this mixed-valent oxide shell is somewhat surprising, given the strong oxidizing conditions of the OER. Perhaps, leaching of Al contributes to the formation of Fe_3O_4 instead of Fe_2O_3. The lack of a sizable amount of FeO, Fe_2O_3, or FeOOH in our sample was conclusively confirmed by the EELS experiments on the Fe-$L_{2,3}$ and O-K edges. Nevertheless, we believe that the very surface of the shell is covered by dynamically exchanging hydroxyl and peroxide groups, according to the proposed OER mechanisms.[20]

These considerations notwithstanding, our studies conclusively show that $AlFe_2B_2$ acts as a pre-catalyst, with the $[Fe_2B_2]$ layers providing a robust support for the *in situ* generated Fe_3O_4 nanoclusters, which act as active sites for the OER catalysis (Fig. 9). A comparison with other non-oxide OER catalysts (borides and phosphides)[10a,18] reveals a remarkably stable and efficient performance of the catalytic system developed in this work (Fig. 10).

Conclusions

In summary, we have established that the layered-structure boride, $AlFe_2B_2$, serves as an excellent OER pre-catalyst, maintaining high electrocatalytic activity for more than 10 days under alkaline conditions. This material, composed of inexpensive and earth-abundant elements, outperforms the well-known PGM-based catalysts, IrO_2 and RuO_2. The high OER activity of $AlFe_2B_2$ is explained by its ability to act as a robust support for *in situ* formed Fe_3O_4 nanoclusters, which serve as active catalytic sites. This notion is supported by the much poorer performance of the catalyst prepared solely with Fe_3O_4 nanoparticles, as well as by electron microscopy studies, which clearly demonstrate the fast formation of the Fe_3O_4 shell on the surface of the $AlFe_2B_2$ particles upon initial electrocatalytic cycling.

It is also possible that the Al layers not only separate the $[Fe_2B_2]$ layers and thus provide a more structured pre-catalyst, but also act as efficient electron-transport pathways, thus additionally facilitating the electrocatalytic reaction. To address this possibility, as well as other intriguing questions raised by the present work, we are currently expanding our studies to the other AlM_2B_2 (M = Cr, Mn) compounds, which are isostructural to $AlFe_2B_2$. Our findings in this direction will be reported in due course.

Author Contribution

The manuscript was written through contributions of all authors. All authors have given approval to the final version of the manuscript.

Conflicts of interest

There are no conflicts to declare.

Abbreviations

BET	Brunauer–Emmett–Teller
COHP	Crystal orbital Hamilton population
ED	Electron diffraction
EDX	Energy dispersive X-ray
EELS	Electron energy loss spectroscopy
FT	Fourier transform
HAADF-STEM	High-angle annular dark-field scanning transmission electron microscopy
HER	Hydrogen evolution reaction
HRTEM	High-resolution transmission electron microscopy
OER	Oxygen evolution reaction
PGM	Platinum group metal
PXRD	Powder X-ray diffraction
RHE	Reversible hydrogen electrode
SCE	Saturated calomel electrode
TEM	Transmission electron microscopy
TOFs	Turnover frequencies

Acknowledgements

The work performed at Florida State University was supported by the Petroleum Research Fund of the American Chemical Society (award 59251-ND10) and in part by the U.S. National Science Foundation (award DMR-1507233). The work performed at the International Iberian Nanotechnology Laboratory was partially supported by the European Union's Horizon 2020 research and innovation program through the CritCat Project under Grant Agreement No. 686053, and by FROnTHERA (NORTE-01-0145-FEDER-000023) project cofinanced by European Union Funds, through Portuguese NORTE 2020 program. The EELS studies were performed with the financial support from the Agence Nationale de la Recherche in the framework of the "Investissements d'avenir" program with the reference ANR-11-EQPX-0020.

References

1 N. S. Lewis and D. G. Nocera, Powering the planet: Chemical challenges in solar energy utilization, *Proc. Natl. Acad. Sci. U. S. A.*, 2006, **103**, 15729–15735.

2 J. R. McKone, N. S. Lewis and H. B. Gray, Will solar-driven water-splitting devices see the light of day?, *Chem. Mater.*, 2014, **26**, 407–414.

3 I. Roger, M. A. Shipman and M. D. Symes, Earth-abundant catalysts for electrochemical and photoelectrochemical water splitting, *Nat. Rev. Chem.*, 2017, **1**, 0003.

4 (*a*) A. Singh and L. Spiccia, Water oxidation catalysts based on abundant 1st row transition metals, *Coord. Chem. Rev.*, 2013, **257**, 2607–2622; (*b*) J. M. Saveant, Molecular catalysis of electrochemical reactions. Mechanistic aspects, *Chem. Rev.*, 2008, **108**, 2348–2378; (*c*) D. A. Lutterman, Y. Surendranath and D. G. Nocera, A self-healing oxygen-evolving catalyst, *J. Am. Chem. Soc.*, 2009, **131**, 3838–3839; (*d*) J. R. Galán-Mascarós, Water oxidation at electrodes modified with earth-abundant transition-metal catalysts, *ChemElectroChem*, 2015, **2**, 37–50; (*e*) M. S. Burke, L. J. Enman, A. S. Batchellor, S. H. Zou and S. W. Boettcher, Oxygen evolution reaction electrocatalysis on transition metal oxides and (oxy)hydroxides: activity trends and design principles, *Chem. Mater.*, 2015, **27**, 7549–7558; (*f*) S. Jin, Are metal chalcogenides, nitrides, and phosphides oxygen evolution catalysts or bifunctional catalysts?, *ACS Energy Lett.*, 2017, **2**, 1937–1938.

5 C. C. L. McCrory, S. Jung, I. M. Ferrer, S. M. Chatman, J. C. Peters and T. F. Jaramillo, Benchmarking hydrogen evolving reaction and oxygen evolving reaction electrocatalysts for solar water splitting devices, *J. Am. Chem. Soc.*, 2015, **137**, 4347–4357.

6 J. Hwang, R. R. Rao, L. Giordano, Y. Katayama, Y. Yu and Y. Shao-Horn, Perovskites in catalysis and electrocatalysis, *Science*, 2017, **358**, 751–756.

7 L. T. Alameda, C. F. Holder, J. L. Fenton and R. E. Schaak, Partial etching of Al from MoAlB single crystals to expose catalytically active basal planes for the hydrogen evolution reaction, *Chem. Mater.*, 2017, **29**, 8953–8957.

8 L. T. Alameda, P. Moradifar, Z. P. Metzger, N. Alem and R. E. Schaak, Topochemical deintercalation of Al from MoAlB: stepwise etching pathway, layered intergrowth structures, and two-dimensional MBene, *J. Am. Chem. Soc.*, 2018, **140**, 8833–8840.

9 X. Tan, P. Chai, C. M. Thompson and M. Shatruk, Magnetocaloric effect in $AlFe_2B_2$: toward magnetic refrigerants from earth-abundant elements, *J. Am. Chem. Soc.*, 2013, **135**, 9553–9557.

10 (*a*) J. Xu, X.-K. Wei, J. D. Costa, J. L. Lado, B. Owens-Baird, L. P. L. Goncalves, S. P. S. Fernandes, M. Heggen, D. Y. Petrovykh, R. E. Dunin-Borkowski, K. Kovnir and Y. V. Kolen'ko, Interface engineering in nanostructured nickel phosphide catalyst for efficient and stable water oxidation, *ACS Catal.*, 2017, **7**, 5450–5455; (*b*) J. Y. Xu, J. P. S. Sousa, N. E. Mordvinova, J. D. Costa, D. Y. Petrovykh, K. Kovnir, O. I. Lebedev and Y. V. Kolen'ko, Al-induced in situ formation of highly active nanostructured water-oxidation electrocatalyst based on Ni-phosphide, *ACS Catal.*, 2018, **8**, 2595–2600.

11 *X'Pert HighScore Plus software v. 2.2b*, PANalytical B.V., Almelo, Netherlands, 2006.

12 R. Dronskowski and P. E. Blochl, Crystal Orbital Hamilton Populations (COHP) - energy-resolved visualization of

chemical bonding in solids based on density-functional calculations, *J. Phys. Chem.*, 1993, **97**, 8617–8624.

13 R. Tank, O. Jepsen, A. Burkhardt and O. K. Andersen, *The program TB-LMTO-ASA. Version 4.7*, Max-Planck-Institut fur Festkorperforschung, Stuttgart, 1999.

14 W. Jeitschko, Crystal structure of Fe_2AlB_2, *Acta Crystallogr., Sect. B: Struct. Crystallogr. Cryst. Chem.*, 1969, **25**, 163–165.

15 A. L. Patterson, The Scherrer formula for X-ray particle-size determination, *Phys. Rev.*, 1939, **56**, 978–982.

16 P. Chai, S. A. Stoian, X. Y. Tan, P. A. Dube and M. Shatruk, *J. Solid State Chem.*, 2015, **224**, 52–61.

17 Y. V. Kolen'ko, M. Bañobre-López, C. Rodríguez-Abreu, E. Carbó-Argibay, A. Sailsman, Y. Piñeiro-Redondo, M. F. Cerqueira, D. Y. Petrovykh, K. Kovnir, O. I. Lebedev and J. Rivas, Large-scale synthesis of colloidal Fe_3O_4 nanoparticles exhibiting high heating efficiency in magnetic hyperthermia, *J. Phys. Chem. C*, 2014, **118**, 8691–8701.

18 S. Sun, H. Li and Z. J. Xu, Impact of surface area in evaluation of catalyst activity, *Joule*, 2018, **2**, 1024–1027.

19 L. Trotochaud, S. L. Young, J. K. Ranney and S. W. Boettcher, Nickel–iron oxyhydroxide oxygen-evolution electrocatalysts: the role of intentional and incidental iron incorporation, *J. Am. Chem. Soc.*, 2014, **136**, 6744–6753.

20 R. L. Doyle and M. E. G. Lyons, Kinetics and mechanistic aspects of the oxygen evolution reaction at hydrous iron oxide films in base, *J. Electrochem. Soc.*, 2013, **160**, H142–H154.

21 (*a*) J. Masa, P. Weide, D. Peeters, I. Sinev, W. Xia, Z. Sun, C. Somsen, M. Muhler and W. Schuhmann, Amorphous cobalt boride (Co_2B) as a highly efficient nonprecious catalyst for electrochemical water splitting: oxygen and hydrogen evolution, *Adv. Energy Mater.*, 2016, **6**; (*b*) J. Jiang, M. Wang, W. Yan, X. Liu, J. Liu, J. Yang and L. Sun, Highly active and durable electrocatalytic water oxidation by a $NiB_{0.45}/NiO_x$ core-shell heterostructured nanoparticulate film, *Nano Energy*, 2017, **38**, 175–184; (*c*) W.-J. Jiang, S. Niu, T. Tang, Q.-H. Zhang, X.-Z. Liu, Y. Zhang, Y.-Y. Chen, J.-H. Li, L. Gu, L.-J. Wan and J.-S. Hu, Crystallinity-modulated electrocatalytic activity of a nickel(II) borate thin layer on Ni_3B for efficient water oxidation, *Angew. Chem., Int. Ed.*, 2017, **56**, 6572–6577; (*d*) J. M. V. Nsanzimana, Y. Peng, Y. Y. Xu, L. Thia, C. Wang, B. Y. Xia and X. Wang, An efficient and earth-abundant oxygen-evolving electrocatalyst based on amorphous metal borides, *Adv. Energy Mater.*, 2017, **8**, 1701475; (*e*) H. Chen, S. Ouyang, M. Zhao, Y. Li and J. Ye, Synergistic activity of Co and Fe in amorphous Co_x–Fe–B catalyst for efficient oxygen evolution reaction, *ACS Appl. Mater. Interfaces*, 2017, **9**, 40333–40343; (*f*) N. Xu, G. Cao, Z. Chen, Q. Kang, H. Dai and P. Wang, Cobalt nickel boride as an active electrocatalyst for water splitting, *J. Mater. Chem. A*, 2017, **5**, 12379–12384; (*g*) J. Zhang, X. Li, Y. Liu, Z. Zeng, X. Cheng, Y. Wang, W. Tu and M. Pan, Bi-metallic boride electrocatalysts with enhanced activity for the oxygen evolution reaction, *Nanoscale*, 2018, **10**, 11997–12002; (*h*) J. Xu, J. Li, D. Xiong, B. Zhang, Y. Liu, K.-H. Wu, I. Amorim, W. Li and L. Liu, Trends in activity for the oxygen evolution reaction on transition metal (M = Fe, Co, Ni) phosphide pre-catalysts, *Chem. Sci.*, 2018, **9**, 3470–3476.